LAWRENCE
LIVERMORE
NATIONAL
LABORATORY

LLNL-JRNL-654765

Radiative Snowflake Divertor Studies in DIII-D.

V. A. Soukhanovskii

May 22, 2014

Journal of Nuclear Materials

Disclaimer

Radiative Snowflake Divertor Studies in DIII-D. ☆

V. A. Soukhanovskii[a,*], S.L. Allen[a], M.E. Fenstermacher[a], D.N. Hill[a], C.J. Lasnier[a], M.A. Makowski[a], A.G. McLean[a], W.H. Meyer[a], E. Kolemen[b], R. J. Groebner[c], A.W. Hyatt[c], A. W. Leonard[c], T. H. Osborne[c], T.W. Petrie[c]

[a]*Lawrence Livermore National Laboratory, Livermore, CA 94550, USA*
[b]*Princeton Plasma Physics Laboratory, Princeton, NJ 08543, USA*
[c]*General Atomics, San Diego, CA 92186, USA*

Abstract

Recent DIII-D experiments assessed the snowflake divertor (SF) configuration in a radiative regime in H-mode discharges with D_2 seeding. The SF configuration was maintained for many energy confinement times (2-3 s) in H-mode discharges (I_p = 1.2 MA, P_{NBI} = 3 − 5 MW, and $B \times \nabla B$ down), and found to be compatible with high performance operation (H98y2≥ 1). Even though the two studied SF configurations, the SF-plus and the SF-minus, have a different placement of the secondary null (private flux vs common flux, respectively), and differences in the magnetic geometry and effects on particle and heat transport, similar results were obtained. The stored energy lost per ELM was reduced, and significant divertor heat flux reduction between and during ELMs was observed over a range of collisionalities, from lower density conditions toward a higher density H-modes with the radiative SF divertor.

Keywords: JNM keywords: P0500 Plasma-Materials Interaction, P0600 Plasma Properties
PSI-20 keywords: Divertor, Divertor plasma, Power deposition, ELM, DIII-D
PACS: 52.55.Fa Tokamaks, 52.55.Rk Power exhaust; divertors

1. Introduction

A snowflake divertor (SF) configuration [1] has been proposed as a potental solution for the tokamak divertor power exhaust problem. The SF divertor magnetic configuration uses a second-order null created by merging two first-order nulls of the standard divertor [1, 2]. Poloidal magnetic flux surfaces in the region of the exact second-order null have six hexagonal separatrix branches with an appearance of a snowflake. The exact second-order null configuration is topologically unstable [1]. In the experiment, two variants of the exact configuration called snowflake-plus and snowflake-minus are often realized in steady-state. In the SF-plus, the secondary null is on the private flux region side of the standard divertor X-point. In the SF-minus, the secondary null approaches the standard divertor X-point from the common flux scrape-off layer (SOL) side. In the SF configurations, the region of low poloidal field B_p surrounding the null(s) (Figure 1) is broader (cf. standard divertor) and has a strong impact on edge plasma properties. Experiments performed in the TCV [3, 4], NSTX [5, 6, 7] and DIII-D tokamaks [8] are providing data to support the physics basis for the SF divertor concept development for future high-power facilities. Initial experiments in DIII-D and NSTX at high divertor power density demonstrated significantly reduced divertor heat flux with the SF-minus divertor and compatibility with high performance operation (H98y2≥ 1). In this paper we discuss recent DIII-D experiments where the SF configurations were combined with D_2-seeded H-mode plasmas to assess the SF geometry effects, heat transport, and radiation in the radiative SF-plus and SF-minus divertors. Reduced ELM energies, and greatly reduced divertor inter-ELM and peak ELM heat fluxes were measured in the SF-minus and SF-plus divertor configurations spanning a range of edge and divertor collisionalities (e.g. with attached and partially detached strike points), compatible with high performance H-mode operation.

2. Experimental

The SF divertor configuration experiments were conducted in DIII-D using a standard highly-shaped H-mode discharge scenario with I_p = 1.2 MA and P_{NBI} = 1 − 5 MW, and ion $Bx\nabla B$ direction toward the lower divertor. A divertor cryopump was used for particle removal, and D_2 seeding was used for steady-state density control in the range $(0.4 - 0.7) \times n_e/n_G$ ($\sim 4.5 - 7.5 \times 10^{19}$ m^{-3} where n_G is the Greenwald density [9]). The DIII-D tokamak divertor is an open geometry divertor with graphite plasma-facing components and divertor heat fluxes of several MW/m^2.

Snowflake configurations were obtained using three existing poloidal field shaping coils in the divertor region. The SF-minus configuration used a combination of a pre-programmed coil current and strike point position control by the plasma control system (as in [6]), while the SF-plus was explicitly controlled through a recently developed algorithm [10]. Both configurations were produced for long periods exceeding energy

☆Paper O-28. LLNL-JRNL-654765

*Presenting and corresponding author. Address: P. O. Box 808, L-637, Lawrence Livermore National Laboratory, Livermore, CA 94551, USA. Email: vlad@llnl.gov

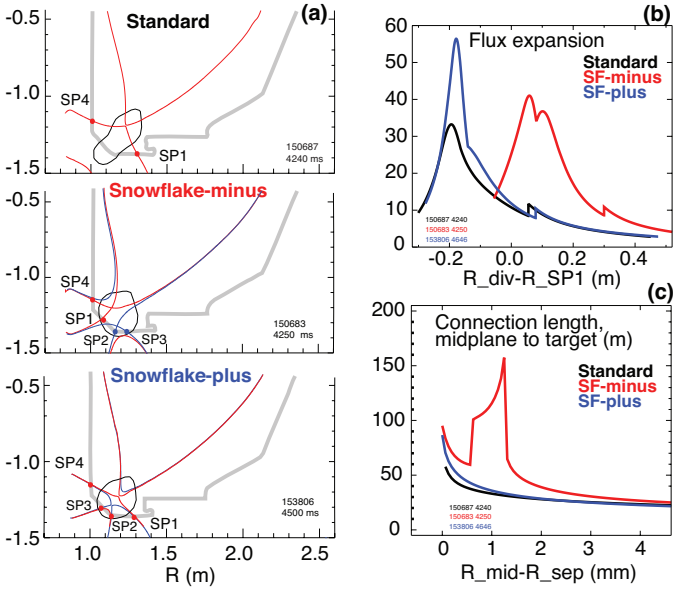

Figure 1: Equilibria of the standard, SF-minus, and SF-plus divertor configurations (a). The primary separatrix is shown in red, the secondary in blue. The region of low $B_p \leq 0.1|B_p/B_{pm}|$ is also shown. (b) Magnetic flux expansion f_{exp} profile vs divertor distance from strike point SP1. (c) Midplane-to-target connection length $L_\parallel$ (c) profile vs radial distance from separatrix remapped to the outer midplane radius (cf. λ_q).

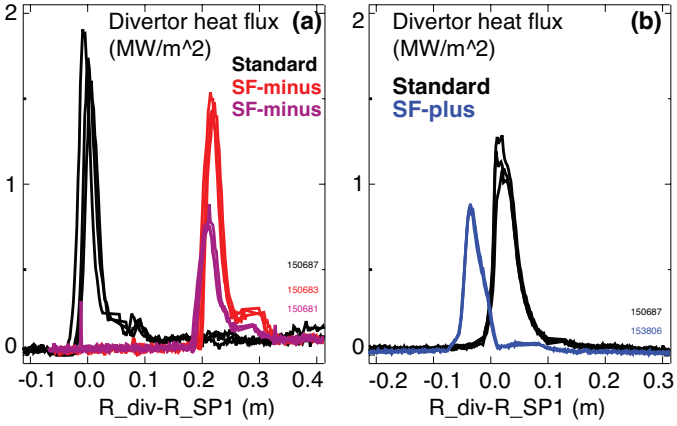

Figure 2: Inter-ELM divertor heat flux profiles in the standard, SF-minus (a) and SF-plus (b) configurations in $P_{NBI} = 4$ MW H-mode discharges at lower n_e.

confinement time $\tau_E \leq 0.250$ s and comparable with discharge duration of 5 – 6 s. Examples of the standard divertor, SF-plus and SF-minus magnetic equilibria with their additional strike points (SP) are shown in Fig. 1. Magnetic equilibria were reconstructed using the standard Grad-Shafranov based equilibrium code EFIT. Magnetic field structure and geometric properties of the SF-plus and the SF-minus are similar to those of the exact SF configuration when the distance D between the poloidal nulls satisfies $D \leq a\ (\lambda_q/a)^{1/3}$ (where a is the minor radius and λ_q is the SOL power width (projected to midplane)) [2]. For the SF divertor discharges used in this study the calculated distance was about 10 cm, while in the experiment the distance $D \leq 10$ cm was typically realized, so it was expected that the SF-plus and the SF-minus would behave much like the exact SF. If the distance D measured in the divertor is remapped via ψ_N to the midplane, as is done with the dr_{sep} parameter in double-null magnetic configurations, one obtains $d_{XX} \leq 1 - 2$ mm (cf. SOL power width $\lambda_q = 2.5 - 3$ mm [11]).

3. Results

Impact of magnetic geometry on divertor inter-ELM heat fluxes. Significant divertor geometry benefits were realized in the SF divertor experiments, affecting divertor power spreading. The realized SF properties included: additional strike points, increased connection length $L_\parallel$, increased plasma-wetted area $A_{wet} = 2\pi R_{SP} f_{exp} \lambda_q$ (where f_{exp} is the poloidal magnetic flux expansion), and increased specific divertor volume (proportional to $L_\parallel$). These points are illustrated in Fig. 1 where the typical standard and SF divertor configurations, the extent of the low B_p region, and the f_{exp} and $L_\parallel$ radial profiles are compared. In the SF-plus and SF-minus configurations, the zone of low B_p was broad and encompassed additional divertor legs and strike points, potentially leading to a much larger region with high poloidal beta, where fast convective plasma redistribution driven by toroidal curvature-driven flute-like modes [2] could take place. In the SF-plus, an additional SOL layer was formed in the private flux region, and the secondary null mainly affected the geometry at the separatrix, within $\leq 10 - 20$ % of the SOL width of 3 mm (in 1.2 MA discharges). The plasma-wetted area (flux expansion) and the connection length increase were modest (10-30 %). In the SF-minus, the secondary null separated the SOL into two manifolds. In the manifold formed between the primary and secondary separatrices (nulls), heat flow was significantly affected by the geometry as both the f_{exp} and $L_\parallel$ were increased by up to 70 %. In the second, outside SOL manifold, the geometry was modified to a lesser extent.

These magnetic geometry modifications led to heat flux reduction and power spreading in the divertor. Shown in Fig. 2 are the outer divertor heat flux profiles measured in H-mode discharges with $P_{NBI} = 4$ MW and at low $n_e \sim (5 - 6) \times 10^{19}$ m^{-3}. The inter-ELM profiles are sampled during the last 10 % of the inter-ELM cycle, i.e. before the ELM when the heat flux is fully relaxed. Three typical profiles are shown for each configuration, sampled within 100-200 ms between 4 and 5 s of each discharge, at n_e exactly matched between the standard and the SF discharges. In the SF-minus, heat flux in the main separatrix strike point was measured only at much higher input power (e.g. at $P_{NBI} \sim 11$ MW [12]), or during ELM transients. The peak heat flux reduction in the additional outer strike point was to a large extent dominated by the A_{wet} factor, and varied within 50 %, as shown in 2 (a), for seemingly identical discharge conditions. In the SF-plus, the A_{wet} impact on the heat deposition in the primary separatrix strike point was minimal, suggesting that other geometry (aside from the A_{wet}) and/or transport effects contributed to the heat flux reduction. The inner (vertical) target heat fluxes were affected in a similar manner.

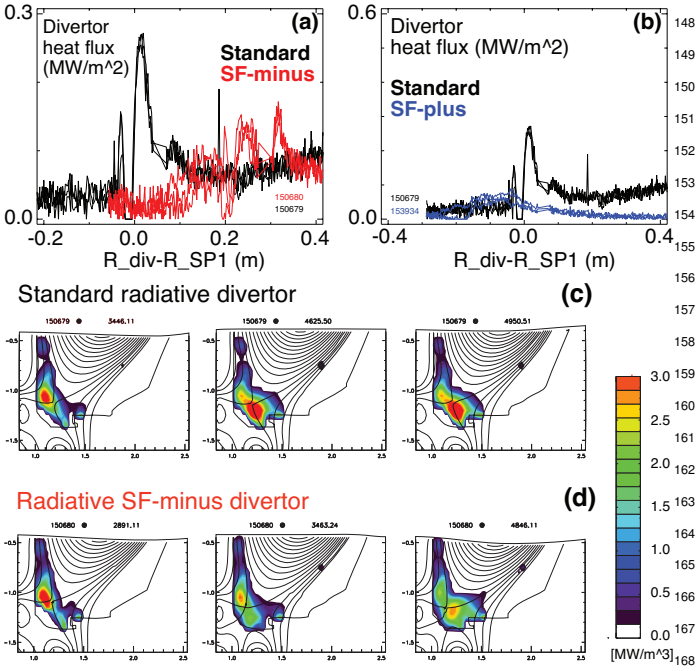

Figure 3: Inter-ELM divertor heat flux profiles in the standard radiative, SF-minus (a), and SF-plus (b) divertors. Radiated power density distribution during a transition to radiative divertor in the standard (c) and SF-minus (d).

Radiative SF Divertor. The SF geometry could lead to a facilitated access to the strike points detachment due to increased volumetric power and momentum losses, as apparently was the case in the NSTX SF-minus experiments [6]. Radiative divertor conditions in DIII-D are routinely accessed with carbon and deuterium radiation using D_2 seeding that increases upstream (and core) density [13, 14].

Initial radiative SF divertor experiments demonstrated that 1) both the radiative SF-plus and SF-minus were compatible with the H-mode confinement albeit with some confinement degradation; 2) the reduction of inter-ELM divertor heat fluxes was stronger in the SF configurations; 3) carbon and deuterium emissions were more broadly distributed in the SF configurations, including the additional divertor legs; 4) the onset of radiative SF conditions (e.g., increase in impurity radiation and recombination, heat flux reduction) were obtained at similar core n_e as in comparable discharges with the standard divertor.

While the confinement degradation was not associated with the SF formation at lower-to-medium densities, additional D_2 seeding at rates 50-80 Torr l/s (to raise the density for radiative divertor onset) resulted in 10-20 % reduction in, e.g., H98(y,2) and H89L factors and plasma stored energy W_{MHD} in the standard divertor, and in additional 10-20 % in H-mode discharges with the radiative (higher-density) SF-plus or SF-minus. The degradation was associated with the reduction of pedestal T_e^{ped} and pedestal energy $W_{ped} = 3/2 n_e^{ped}(T_e^{ped} + T_i^{ped})V_{plasma} \simeq 3P_e^{ped}V_{plasma}$. Further H-mode scenario development is necessary to optimize compatibility of the core plasma with radiative SF, as is typically done with the standard radiative divertor (e.g., [15]).

Inter-ELM divertor heat flux profiles demonstrated that the radiative SF divertor was more effective in reducing divertor heat flux than the standard divertor at $P_{NBI} = 4 - 5$ MW. The profiles are compared in Fig. 3. In the standard divertor, the partial detachment led to a significant (up to x10) peak heat flux reduction. In the radiative SF-minus and SF-plus, the reduction was greater, leading to a nearly complete power detachment, as heat flux in the trike points was barely detectable.

Divertor radiated power from carbon and deuterium species was distributed more broadly and uniformly in the SF configurations. Shown in Fig. 3 (c, d) are radiated power distributions in the standard and SF-minus divertors as they progress toward highly radiative conditions, obtained from tomographic reconstructions of divertor radiated power measured by multichannel bolometry. The total divertor radiated power was about 2 MW in the radiative standard, SF-plus or minus configurations, differing by 10-15 % (cf. $P_{SOL} \sim 3.0 - 3.5$ MW). In the standard divertor, radiation initially peaked in the inner and outer divertor legs, and eventually the radiative front moved to the X-point (e.g, [14]). In the SF-minus, radiation also initially peaked in the divertor legs, however, as the SF-minus was formed, it was broadly distributed throughout the divertor volume, with occasional peaking at the null-points. In the SF-plus, the radiation front was formed in the divertor legs and moved toward the null-point region where it stabilized. The extended connection length region enabled a broader radiation zone. Importantly, despite the geometry (e.g., increase in $L_\parallel$ by 50-75 %), the SF configurations were not more likely than the standard divertor to form X-point radiative instabilities that can degrade the confinement.

ELM heat flux mitigation. The SF configuration effects on pedestal and SOL led to the reduction of ELM energy and heat deposition on the targets at lower density, and a near complete elimination of ELM heat fluxes in highly radiative conditions.

In the pedestal region, both the magnetic shear and q_{95} were systematically increased by 10-30 % due to the broader region of lower B_p inside the separatrix. Accordingly, the pedestal stored energy lost per ELM ΔW_{ELM} was reduced since the pedestal collisionality $\nu^*_{ped} = \pi R q_{95}/\lambda_{e,e}$ was increased and the ELM parallel transit time $\tau_\parallel^{ELM} = 2\pi R q_{95}/c_{s,ped}$ (the pedestal ion transport time from the mid plane to the target at the sound speed c_s) was increased. This was consistent with the Type I ELM scaling of ΔW_{ELM} with ν^*_{ped} found in many tokamaks [16]. Shown in Fig. 4 are pedestal and ELM characteristics in the standard and the SF-minus divertor discharges at lower densities and at radiative conditions. Kinetic profiles were similar with and without the SF configurations. Pedestal top plasma parameters changed within 5-15 %: with the SF configuration, T_e^{ped} slightly reduced, n_e^{ped} slightly increased, and p_e^{ped} remained nearly constant, as shown in Fig. 4 (a). Pedestal energy W_{ped} was nearly unaffected at lower n_e. However, some additional degradation of the pedestal T_e was noted in highly radiative SF configurations, leading to the pedestal energy reduction (Fig. 4 (a,b)). Changes in the magnetic shear and weak changes in pedestal pressure gradient did not apparently affect the stability of the peeling-balooning modes, as only small changes

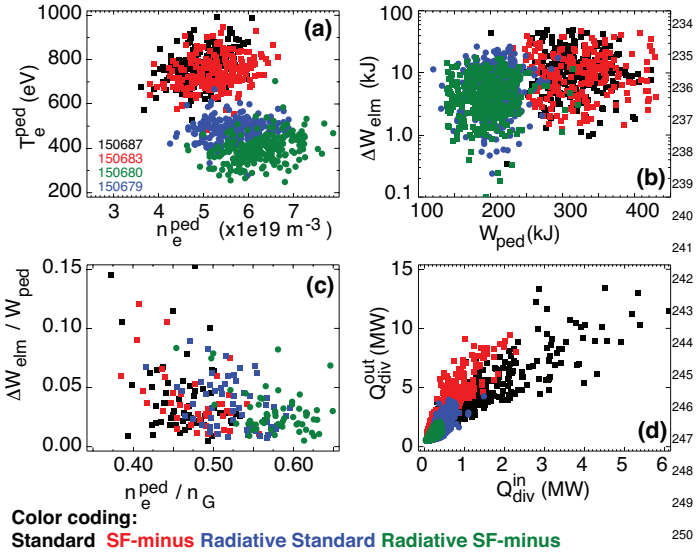

Figure 4: Pedestal and divertor parameters in H-mode discharges with the standard and SF-minus configurations at lower n_e, and the radiative standard and SF-minus divertors at higher n_e. Data sampled between 4 and 5 s. (a) Pedestal operating space, T_e^{ped} vs n_e^{ped}; (b) Stored energy lost per ELM vs pedestal energy; (c) Normalized energy lost per ELM $\Delta W_{ELM}/W_{ped}$ vs pedestal Greenwald density fraction; (d) Divertor power operating space, $Q_{out}(t)$ vs $Q_{in}(t)$.

in ELM frequency (about 10-20 %) were detected with the SF. The stored energy lost per ELM ΔW_{ELM} was reduced in discharges with the SF configurations. In some discharges, the effect was strong, ΔW_{ELM} was reduced by up to 50 % [8]. More typically, however, the reduction was in the range $5-20$ %. At higher density in radiative SF divertor discharges, both the ΔW_{ELM} and $\Delta W_{ELM}/W_{ped}$ were lower by 10-20 % (cf. standard divertor, Fig. 4 (b,c)).

The SF configurations also affected ELM heat transport in the SOL, resulting in reduced peak target temperatures and heat loads. The increased divertor connection length $L_{||}$ reduce the target surface temperature rise as $\Delta T_t \sim W_{ELM}/\sqrt{\tau_d}$, where W_{ELM} is the ELM energy and τ_d is the ELM deposition time which is increased at longer $L_{||}$ [17]. Another possible mechanism is the fast convective transport in the low B_p region driven by instabilities [2] that can lead to the ELM heat flux sharing among the additional strike points. Shown in Fig. 4 (d) is the divertor power operating space, the total power received by the outer (horizontal) target Q_{div}^{out} vs the power received by the inner (vertical) target Q_{div}^{in}, for the four discharges discussed above. The total power is obtained by integrating heat flux profiles measured by infrared thermography. Outer peak powers above 1-2 MW are attributed to ELMs in the standard and SF-minus at lower n_e. The peak powers were reduced in the SF-minus by up to 50-70 %, and further reduced in the radiative SF-minus by up to 50 %, as compared to the standard divertor configurations. Some uncertainties remain as to whether the SF configurations were maintained during equilibria perturbations due to large ELMs. Divertor infrared thermography data suggested that in many cases the SF configurations were not destroyed. In the standard divertor configuration, radiative buffering of ELM divertor heat loads has not been effective (e.g., [18]). Typically, the partially-detached standard divertor strike points re-attach during ELMs enabling significant transient heat and particle fluxes to reach the targets. Radiative SF divertor experiments in DIII-D demonstrated that at increased density (collisionality), both the ΔW_{ELM} and the divertor q_{peak}^{ELM} were reduced stronger than in standard radiative divertor, leading to the much reduced peak powers. A combination of the geometry, transport and enhanced radiative dissipation may provide a significant benefit for ELM buffering. We note that this observation was also made in NSTX radiative SF-minus discharges [7].

In summary, the emerging understanding of inter-ELM and ELM divertor heat transport in the radiative SF divertor from recent DIII-D experiments provides support to the snowflake divertor concept as a promising solution for divertor heat flux mitigation in future magnetic fusion devices. The experiments demonstrated the SF divertor compatibility with high H-mode confinement, radiative divertor with gas seeding, and led to significantly reduced ELM energies, as well as divertor heat fluxes between and during ELMs. Future experiments and analysis will focus on confinement optimization, transport, radiative limit, and cryopumping compatibility studies, as well as magnetic feedback control improvements.

Acknowledgements. We thank the entire DIII-D Team for technical, engineering and computer support as well as plasma and diagnostic operations. Dr. D. D. Ryutov is acknowledged for insightful discussions. This work was performed under the auspices of the US Department of Energy (US DOE) under DE-AC52-07NA27344, DE-AC02-09CH11466, DE-FC02-04ER54698 and DE-AC04-94AL85000.

[1] RYUTOV, D., Phys. Plasmas **14** (2007) 064502.
[2] RYUTOV, D. et al., Plasma Physics and Controlled Fusion **54** (2012).
[3] PIRAS, F. et al., Phys. Rev. Lett. **105** (2010) 155003.
[4] REIMERDES, H. et al., Plasma Physics and Controlled Fusion **55** (2013).
[5] SOUKHANOVSKII, V. et al., Nucl. Fusion **51** (2011) 012001.
[6] SOUKHANOVSKII, V. et al., Phys. Plasmas **19** (2012/08/) 082504 (12 pp.) .
[7] SOUKHANOVSKII, V. et al., Journal of Nuclear Materials **438** (2013) S96 .
[8] HILL, D., Nucl. Fusion **53** (2013/10/) 104001 (18 pp.) .
[9] GREENWALD, M. et al., Nucl. Fusion **28** (1988) 2199.
[10] KOLEMEN, E., This conference **Paper O-18** (2014).
[11] MAKOWSKI, M. A. et al., Phys. Plasmas **19** (2012) 056122.
[12] PETRIE, T. W., This conference **Paper P1-082** (2014).
[13] PETRIE, T. et al., Nuclear Fusion **37** (1997) 321 .
[14] FENSTERMACHER, M. E. et al., Plasma Phys. Control. Fusion **41** (1999) A345.
[15] PETRIE, T. et al., Journal of Nuclear Materials **363–365** (2007) 416 , Plasma-Surface Interactions-17.
[16] LOARTE, A. et al., Journal of Nuclear Materials **313–316** (2003) 962 .
[17] ROGNLIEN, T. et al., Journal of Nuclear Materials **438** (2013) S418 .
[18] MONIER-GARBET, P. et al., Nuclear Fusion **45** (2005) 1404.